Performing co-ordinated turns with articulated wing-tips as multi-axis control effectors

P. Bourdin
University of Bristol
Bristol, UK

A. Gatto
Alvin.Gatto@brunel.ac.uk
Brunel University
Uxbridge, UK

M. I. Friswell
Swansea University
Swansea, UK

ABSTRACT

This paper investigates a novel method for the control of aircraft. The concept consists of articulated split wing-tips, independently actuated and mounted on a baseline flying wing. The general philosophy behind the concept was that adequate control of a flying wing about its three axes could be obtained through local modifications of the dihedral angle at the wing-tips, thus providing an alternative to conventional control effectors such as elevons and drag rudders. Preliminary computations with a vortex lattice model and subsequent wind tunnel tests and Navier-Stokes computations demonstrate the viability of the concept for co-ordinated turns, with individual and/or combined wing-tip deflections producing multi-axis, coupled control moments. The multi-axis nature of the generated moments tends to over-actuate the flight control system, leading to some redundancy, which could be exploited to optimise secondary objective functions such as drag or bending moment.

NOMENCLATURE

b wing span
C_l, C_m, C_n rolling, pitching and yawing moment coefficients
C_{Di} lift-induced drag coefficient
C_{Lx} lift coefficient derivative with respect to parameter x
C_{lx}, C_{mx}, C_{nx} rolling, pitching and yawing moment coefficient derivatives with respect to parameter x
D, C_D drag, drag coefficient
g gravitational acceleration

L, C_L lift, lift coefficient
R turn radius
S   reference wing area
V_{cg} velocity of the wing centre of gravity
W aircraft weight

Symbols

α angle-of-attack
γ_{Aft} dihedral angle of the aft wing-tips (positive for up wing-tip, zero in wing plane)
γ_{LF} left fore wing-tip dihedral angle (positive for up wing-tip, zero in wing plane)
γ_{RF} right fore wing-tip dihedral angle (positive for up wing-tip, zero in wing plane)
Ω turn rate
ϕ bank angle
ρ air density

1.0 INTRODUCTION

Over the past century, aircraft designers and manufactures have made huge strides in the advancement of aircraft technologies. From the days of the first powered, controlled flight, in 1903 by the Wright brothers[1] which extended only 120 feet between take-off and landing, to the fastest crossing of the continental United
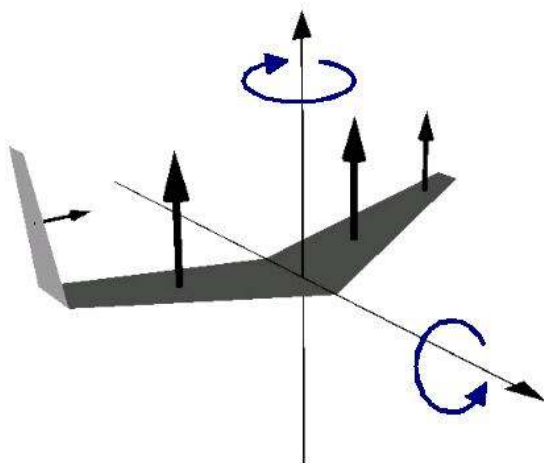
Figure 1. An asymmetric wing-tip folding for a
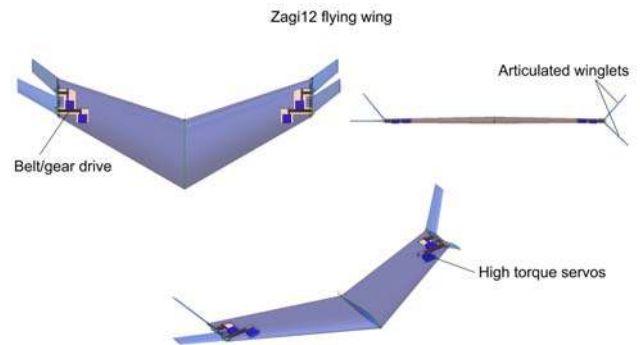sweptback wing to initiate a co-ordinated turn.

Figure 2. Wind-tunnel model and its internal structure.

States in 1990 by the revolutionary and exceptional, Lockheed Martin SR-71 'Blackbird', the aircraft as a viable platform has and continues to, develop at an impressive rate. One future vision for the next step in this impressive advancement timeline is the aptly named 'morphing aircraft'. In the future, these aircraft could be purposely designed and engineered to change between multiple, dissimilar 'states', giving an overall enhanced efficiency and operational effectiveness unmatched by even today's standards. This ability, if realised, would allow one platform to perform multiple, dissimilar mission objectives, which currently, may require multiple aircraft types with implications for procurement cost, in-service support needs and cost of operation. However, although the intended benefits for this next generation aircraft concept are obvious, the added complexity and control requirements of this type of platform clearly presents substantial challenges to current aircraft design. Critically therefore, it is of paramount importance that investigations into the development of new and novel methods of aircraft control are rigorously explored.

Some of the more current morphing wing/aircraft concepts have dealt with different aspects of flight control and/or multiple mission adaptability[2-9]. Morphing for flight control involves primarily, small, continuous adjustments in the shape of the wing[3-5] and/or surrounding flowfield[6] to manoeuvre the aircraft during flight. Morphing for mission adaptation involves making greater shape changes in order to optimise, in flight, the wing characteristics for the current flight condition[7-9]. These different applications are all regarded as morphing, however each is very different in terms of the magnitude of the shape changes required and time constants necessary for these changes. Fortunately large changes for improved performance are only required at low frequency and fast changes for flight control only need to be small amplitude. This does mean that there is never going to be a single solution for a morphing aircraft and the technology employed will be vastly different depending on the application required. However, all applications require that morphing achieves the objective of improved performance and/or functionality. Often this improvement will be at the expense of increased weight and complexity and the performance improvement must account for this. Seigler et al[10] gave a good summary and history of morphing technology and Campanile[11] discussed the challenge of introducing flexibility into wing structures.

The structural technologies available to achieve shape changes in a morphing aircraft fall into two major categories, namely planform changes using rigid mechanisms[8-10] and compliance (for example wing twist or compliant mechanisms)[11-12]. Significant aerodynamic performance gains are only really achievable through large overall changes in the aircraft geometry via wing sweep, area and/or span. Methods for configuration morphing (that is significant planform changes) include wing extension, wing folding or wing sweep. The application of morphing to flight control usually involves small to medium geometric wing changes such as the use of deployable slats and flaps as well as wing warping techniques to enhance the control authority of the aircraft. Other basic morphing motions for seamless flight control include wing twist, wing camber change, or asymmetric wing extension. At present, in both of the technological categories, such medium to large scale changes are obtained with complex and sophisticated mechanical devices significantly increasing the installation and maintenance costs as well as the structural weight of the airframe. It is clear therefore, that substantial gains in these areas could be made if alternative methods to enact these changes were found.

In this paper, we take the view of meso-scale morphing for control, investigating a flying-wing concept using independently-controllable, articulated, split wing-tips to achieve basic manoeuvres. Using such folding, split wing-tips in this regard disrupts significantly the spanwise and chordwise loading, resulting in, conceivably, a more efficient method of lateral, directional and longitudinal control than through the articulation of discrete control surfaces into the mainstream.

The present concept is in fact an extension of a previously-investigated concept[13], where the tips of a flying wing were folded either symmetrically or unsymmetrically to achieve either longitudinal trimming or co-ordinated turns (Fig. 1). Though it appeared to be effective, a single pair of folding wing-tips could not substitute for all the conventional control surfaces at the same time if one wanted to obtain a full control envelope: in particular, to perform level turns at arbitrary bank angles, the wing-tip deflection needed to be combined with some use of elevator to trim the aircraft. The present concept is thus an attempt to control the wing solely with folding wing-tips, removing the elevator from the control line by using a second pair of folding wing-tips (see Fig. 2). With four multi-axis effectors, the aircraft is then over-actuated, leading to some redundancy in the flight control system, which could be exploited to optimise secondary objectives (e.g. minimum drag, minimum bending moment) at fixed lift and moments.

Figure 3. Butt-plane cuts at the wing root and at the winglet root for the planar configuration, showing the aerofoil sections (the air flow would come from the right).
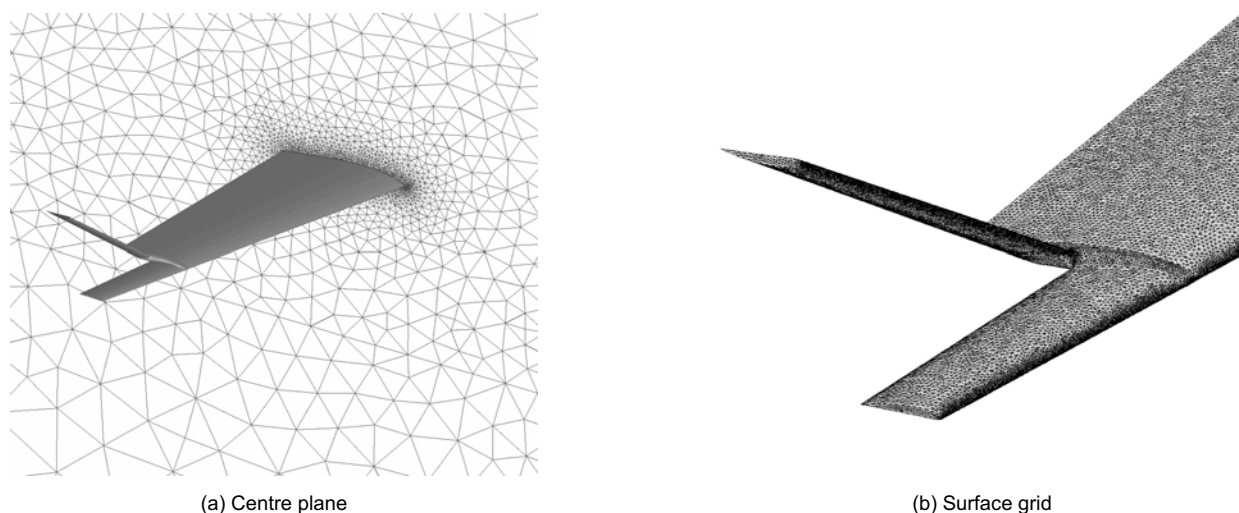

| (a) Centre plane | (b) Surface grid |

Figure 4. Unstructured grid for RANS computations.

2.0 CHARACTERISTICS OF THE INVESTIGATED AIRFRAME

2.1 Geometry

The model used for experimental testing was constructed of a blue foam core with a carbon fibre skin. The unmodified baseline configuration consisted of a planar trapezoidal wing with 30° leading edge (LE) sweep, with aspect and taper ratios of 4·6 and 0·56 respectively. The wing was untwisted and lofted with a 12% thick Zagi aerofoil section with reflexed trailing edge (TE). Modifications to this baseline configuration were primarily performed at the tips through the addition of servo driven articulated hinges where the split wing-tips were fixed. The assembly of the wing/wing-tip interface conserved the LE sweep angle for the fore wing-tips, with the aft wing-tip pair swept at an additional 7°. Each element (fore and aft) of the split wing-tip was a trapezoidal, untwisted winglet of aspect and taper ratios of 2·9 and 0·73 respectively, lofted with NACA 4412 aerofoils. A schematic of the experimental wing model is shown in Fig. 2. Note that the rear winglet aerofoils were turned upside down (i.e. they had negative camber, see Fig. 3). This

particular arrangement was not arbitrary but came from a numerical parametric study with the vortex lattice method presented in 3.1. The goal of that preliminary analysis was to find a suitable arrangement of aerofoil camber for the wing-tips so that they could provide substantial roll and pitch moments given the prescribed control allocation scheme (described below).

2.2 Control allocation scheme

As mentioned in the introduction, with four control effectors and only three moments to control, the system is explicitly over-actuated. To further complicate this situation, the multi-axis moments generated by the present effectors make the system implicitly over-actuated, that is even if the number of effectors is smaller or equal to the number of control moments, there may exist multiple combinations of effector states generating the same control moments. Another particular issue might perhaps be that some types of manoeuvre could involve very different control states, making any transition difficult or causing the flight control system to randomly flip between states. To avoid such a potential issue[†] and to make our analysis of the concept simpler, we decided to actuate the rear winglets in tandem: the number of control lines was thus reduced by

---

[†] To properly address this issue a range of different types of manoeuvre should be considered. However this is not done in the paper where the co-ordinated turn is the manoeuvre of primary interest.

(a) Front view

(a) Rear 3/4 view

Figure 5. Experimental model as mounted in the wind tunnel.

one (i.e. no more explicit over-actuation). The following control allocation scheme was then prescribed: the rear winglets were always deflected symmetrically, acting as the primary pitch effector, while each front winglet could be deflected independently of the others, acting primarily as a roll/yaw effector.

3.0 ANALYSIS TOOLS

3.1 Reduced-order mathematical model

To provide most performance and stability estimates, we relied on a vortex lattice representation of the wing (the so-called vortex lattice method – VLM). In that linearised, potential flow model, angle of attack and sideslip are assumed to be small and the lifting surfaces and their trailing wakes are modelled as a discrete set of horseshoe vortex filaments stacked along the span and chord axes. The spanwise and chordwise loadings are computed by solving a system of linear equations that enforce a flow-tangency condition at specified control points on the wing (the centroid of each bound ring-vortex). All the horseshoe vortices belonging to the same spanwise strip are co-planar, so the sectional camber is modelled by tilting the normal vector at the control point when applying the flow-tangency boundary condition (thin profile approximation). The forces and moments are obtained from the solved load distribution by applying the gener-alised Kutta-Joukowski theorem[14]. Providing that the dimensionless roll rates and reduced frequencies are slow enough, this steady-state aerodynamic model can be used to predict the instantaneous perfor-mance (viscous drag aside) and quasi-static stability derivatives during a rotary or oscillatory motion of the wing.

With regard to the articulated wing-tips, the corresponding control derivatives were obtained from finite differences by perturbating the aerodynamic grid. Otherwise, stability derivatives were computed from a differentiated form of the Kutta-Joukowski theorem (the vortex strength sensitivities stemming from the differentiation were estimated by solving the linear system several times, assuming in turn unit rotation or translation velocity along each body-axis).

All the computations were based on the following uniform discreti-sation, which gave results in the asymptotic range of the method (grid-independent solution range): 19 horseshoe vortices along the span of each winglet and 7 along its chord; 50 horseshoe vortices along each semi-span of the baseline wing and 14 along its chord.

3.2 Higher-order mathematical model

The Reynolds-Averaged Navier-Stokes (RANS) incompressible flow model was used to enable a more precise physical represen-tation within the simulations and to double-check the VLM predic-tions. Because of their cost, RANS computations were only applied to a limited number of cases. Furthermore the RANS numerical flow was fully turbulent whereas the experimental flow was very likely to be transitional.

3.2.1 Discretisation

The open-source field operation and manipulation (OpenFOAM[15]) C++ class library for continuum mechanics was used for solving sequentially the cell-centred, finite volume approximation of the RANS equations on a collocated, unstructured grid, by means of a projection method. The SIMPLE algorithm[16] was chosen to enable the pressure-velocity coupling between momentum and continuity. We selected the one-equation eddy-viscosity model of Spalart-Allmaras (SA)[17] to achieve a first-order closure of the turbulent flow equations. To ensure global second order accuracy in space, viscous fluxes were approximated with central discretisation schemes, convective fluxes with limited linear upwind schemes and gradients with a distance-weighted least-squares fit. Lift and drag forces were obtained from the integration of the pressure and viscous stresses over the wing surface.

3.2.2 Computational domain

The computational grid system was made of tetrahedral elements, except near the wing walls where a prismatic layer of 15 rows was extruded off the underlying surface grid made of 170,000 triangles (see Fig. 4). In total there were approximately three millions cells, with half of them located in the prismatic layer. A posteriori estimates of y_+, the distance to the wall in wall units, indicated the first row of cells off the wall was well within the viscous sub-layer at the simulated Reynolds number (Re) of $3·18 \times 10^5$, with average y^+ values of 1 or smaller and maximum values of approximately 5 near the leading edge of the aft-winglet root aerofoil. To ensure the grid was fine enough, another volume grid generated off a two times denser surface grid was also used to compute the $\gamma_{Aft} = \gamma_{LE} = \gamma_{RF} = 0°$ case (fully planar configuration); differences in predicted lift and drag between both grids were less than 3%, so the initial grid density was deemed acceptable. The far-field (outer) boundary was located

85 mean-aerodynamic-chords away from the wing surface, as advised by Vassberg et al[18] to minimise the influence of the far-field boundaries on the numerical flow solution near the vicinity of the wing. Wherever the flow entered the domain, the flow velocity vector, $\tilde{V}$ and the SA modified eddy viscosity, $\tilde{v}_t$, were prescribed (with $\tilde{v}_t = 5v$) while the pressure, p, was extrapolated from the interior cell-centres. Wherever the flow left the domain, $\tilde{V}$ and $\tilde{v}_t$ were extrapolated from the interior cell-centres while p was prescribed.

3.3 Experimental model

The model was installed inside the closed test section (2·1m × 1·5m, see Fig. 5) of a closed circuit wind tunnel whose maximum operating freestream velocity was 60ms⁻¹. The model was investi-gated at a flow speed of 20(±0·5)ms⁻¹, giving a Reynolds number of $3·18 × 10^5$ based on the mean aerodynamic chord of the planar configuration. At this Reynolds number, the flow is very likely to be transitional, however no boundary layer tripping was used (free transition) for the following reasons: 1) the aerofoil of the main wing (Zagi 12) was designed to operate 'as is', i.e. without turbulators, in that flow regime; 2) the type and location of turbulators and their actual effect on the boundary layer have not yet been well documented, especially at very low Reynolds numbers such as for the flow past the split wing-tips[19]; 3) the addition of turbulators does not always improve the aerofoil performance[19]. Analysed configura-tions included symmetric deflections of the aft wing-tips and unsym-metric deflections of the fore wing-tips, for angles–of–attack ranging from –4° to 16° (with respect to the wing-root chord line). The model was mounted at mid-height in the test section, on top of a support strut connecting the model to a high-frequency dynamic load cell mounted to the underside of the floor of the test section. The freestream turbulence level at the model station was approximately 0·2%. Access to the wind tunnel test section for the support strut was provided by a cutout in the wind tunnel floor which was covered, during wind-tunnel testing, by two thin sheets of fibreboard. Each sheet was constructed to ensure no contact between the supporting strut and the test section was possible. Four high-tension wires were also installed between the active balance plate and the top of the support strut to increase the stiffness of the entire support system, thereby improving the natural frequency characteristics of the combination.

Forces and moments were acquired with a six axis balance (AMTI MC3A-500). The maximum lift, drag and side force capabilities of the cell were ±2kN, ±1kN and ±1kN respectively. Maximum range for the pitching moment, rolling moment and yawing moment were ±56Nm, ±56Nm and ±28Nm respectively. Assessment of the observed non-linearity as well as zero drift after a rigorous pre-testing preparation were found to be better than ±0·5%. All data obtained from the load cell was digitised through a 16-bit dSpace data acquisition system and all data taken over a period of approxi-mately 30 seconds. Control surface position for each winglet was provided by directly-coupled, precision potentiometers purposely built into the model.

All four servos (Digital Hitec HSR-5995TG) used to control the model were driven by a dSpace control system. This system was configured to generate pulse width modulated input signals (50Hz) with variable duty cycles corresponding to a pulse width range of between 400-2,100μs. Calibration of control surface position was carried out using a digital inclinometer (error ±0·1°) positioned on the control surfaces and matched to a readout from the dSpace control system indicating the input signal pulse width. Achievable dihedral angle magnitudes for the wing-tips were –75° to +75° (positive dihedral is up wing-tip, zero dihedral is in the wing plane). The same digital inclinometer was used to calibrate the angle of attack of the model which was measured relative to a flat, prefabricated cut-out at the mid-plane of the wing, co-incident with the chord line.

Figure 6. Attainable pitching moments at 4° and 8° angle-of-attack when the aft wing-tips are deflected in tandem (experimental data, Re = 3·18 x 10⁵, $\gamma_{LE} = \gamma_{RF} = 0°$). Moments are relative moments, with the fully planar configuration as reference.

4.0 RESULTS AND DISCUSSION

In the results presented hereafter the following conventions apply:

● the reference area for all aerodynamic coefficients is the planform area of the fully planar configuration (i.e. the configu-ration with all four wing-tips in the wing plane);

● the span of the planar configuration was used as reference length for the rolling and yawing moments;

● the mean aerodynamic chord of the unmodified, baseline trape-zoidal wing (i.e. the wing without split wing-tips added to it) was used as the reference length for the pitching moments;

● moments are given in the standard stability axes (x forward, y to the right of the pilot, z down) and taken positive according to the right-hand rule about those axes;

● moments are all referenced about the centre of gravity (CG) of the planar configuration, which can be assumed to be the CG of any of the non-planar configuration[†]. The longitudinal position of the CG has been fixed at the foremost location of the aerody-namic centre (at about 73% of the wing root chord, as predicted by the VLM) so as to preserve the static longitudinal stability over the range of permitted wing-tip dihedral angles.

4.1 Attainable moments and rates

4.1.1 Longitudinal control

Control of the longitudinal motion of the flying wing can supposedly be achieved by deflecting the aft winglets in tandem (changing then the effective area of the trimming surfaces), while the fore winglets remain fixed at a given dihedral angle, which we chose to be zero (i.e. in the wing plane). The observed pitching moments for such configurations are plotted versus the aft wing-tip dihedral angle in Fig. 6. One can notice the presence of two monotonic segments in the pitching moment curve: one for negative dihedral angles and the other for positive dihedral angles; both ranging from ±30° to ±75°. In those intervals, the pitching moment increases, almost linearly, with the magnitude (absolute value) of the dihedral angle. This indicates the feasibility of controlling the longitudinal attitude of the airframe: by setting both aft winglets at an intermediate dihedral angle in those intervals (say ±50°, redesigning eventually the TE

† Since wing-tips are rotated about an axis parallel to the wing-root chord line, the chordwise location of the airframe CG remains unchanged during this transformation. Only its spanwise and vertical locations will change. However due to the small mass of the wing-tips relative to the baseline wing, the spanwise and vertical shifts remain insignificant and are less than 1% of the wing-root chord. Therefore assuming the CG is the same for all the configurations is legitimate.
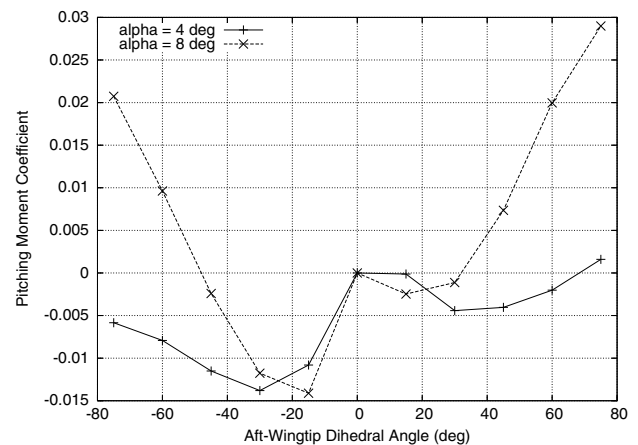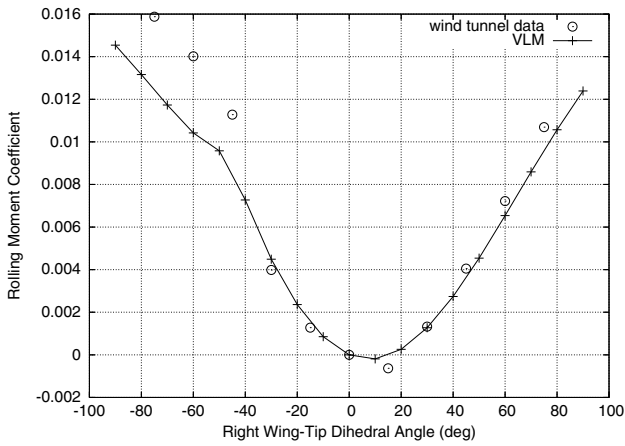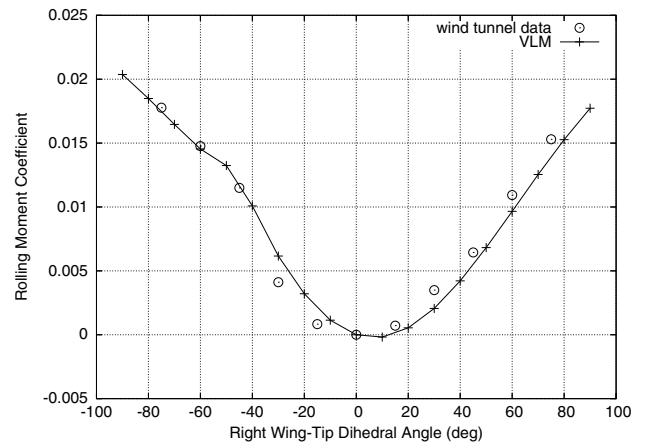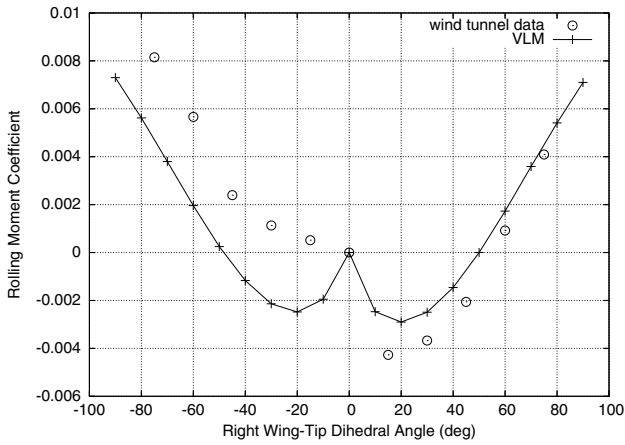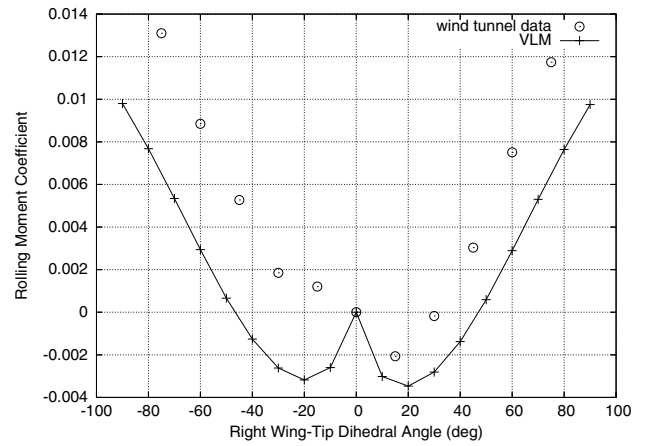
(a) $\gamma_{Aft} = -45°$, $\alpha = 4°$

(b) $\gamma_{Aft} = -45°$, $\alpha = 8°$

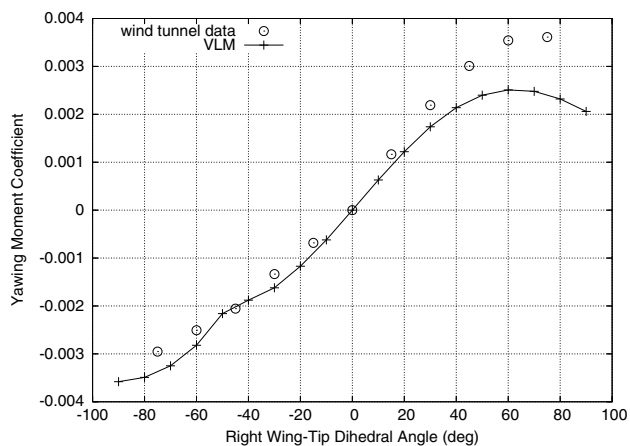(c) $\gamma_{Aft} = 0°$, $\alpha = 4°$

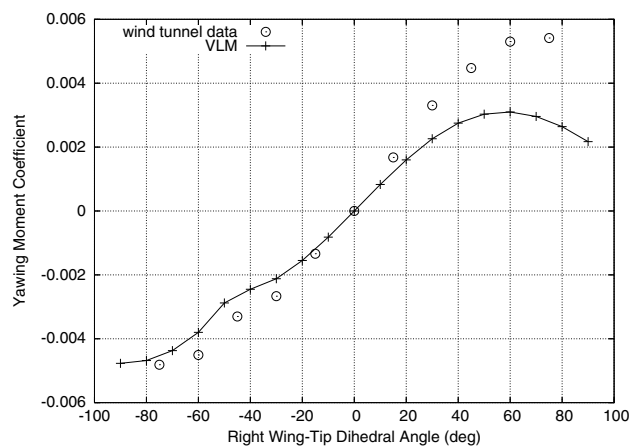(d) $\gamma_{Aft} = 0°$, $\alpha = 8°$

(e) $\gamma_{Aft} = -45°$, $\alpha = 4°$

(f) $\gamma_{Aft} = -45°$, $\alpha = 8°$
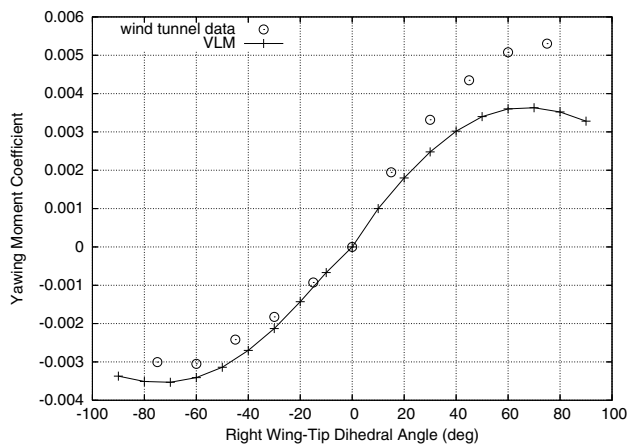
Figure 7. Attainable rolling moments from experimental and numerical data (VLM, RANS and wind-tunnel tests at Re = 3·18 x 10^5) at 4° and 8° angle-of-attack for $\gamma_{LE} = 0°$, $\gamma_{Aft} = \{-45°, 0°, +45°\}$ and γ_{LE} in [–90°, 90°](the angle-of-attack value effectively used during the VLM and RANS computations was adjusted so that the observed and predicted lift coefficients match when $\gamma_{LE} = \gamma_{RF} = 0°$).
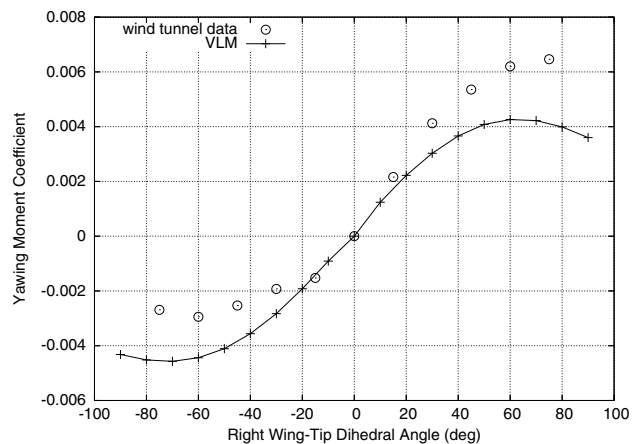
(a) $\gamma_{Aft} = 45°$, $\alpha = 4°$

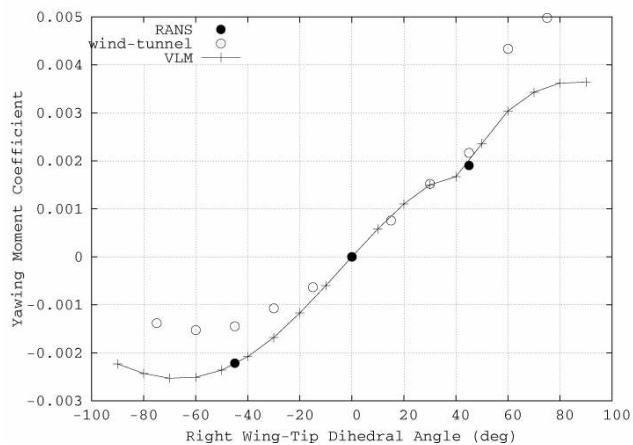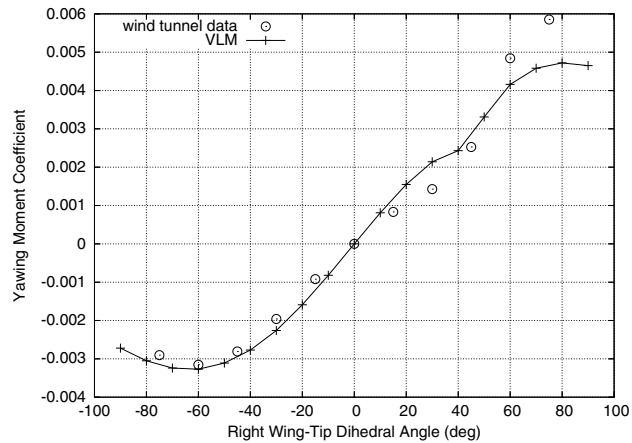(b) $\gamma_{Aft} = -45°$, $\alpha = 8°$

(c) $\gamma_{Aft} = 0°$, $\alpha = 4°$

(d) $\gamma_{Aft} = 0°$, $\alpha = 8°$
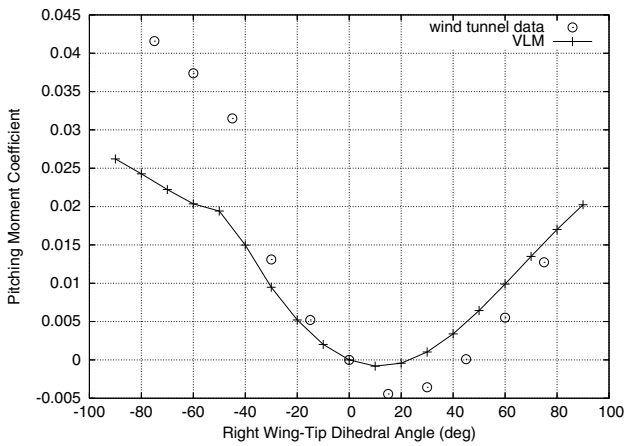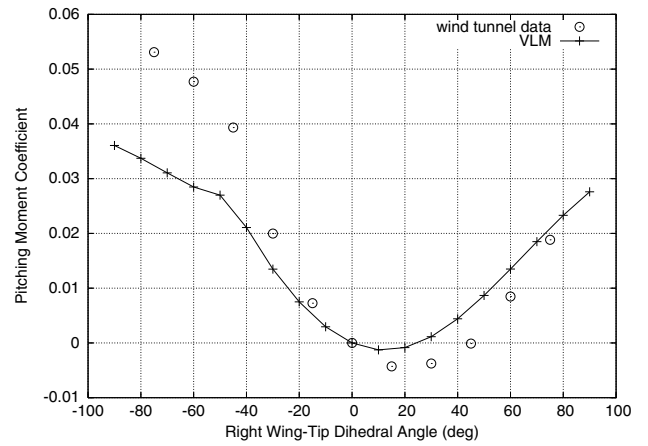
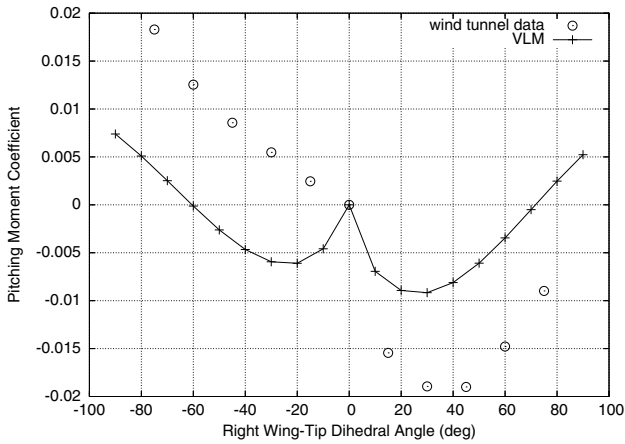(e) $\gamma_{Aft} = 45°$, $\alpha = 4°$

(f) $\gamma_{Aft} = 45°$, $\alpha = 8°$

Figure 8. Attainable yawing moments from experimental and numerical data (VLM, RANS and wind-tunnel tests at Re = 3·18 x 10⁵) at 4° and 8° angle-of-attack for $\gamma_{LE} = 0°$, $\gamma_{Aft} = \{-45°, 0°, +45°\}$ and γ_{RF} in [–90°, 90°](the angle-of-attack value effectively used during the VLM and RANS computations was adjusted so that the observed and predicted lift coefficients match when $\gamma_{LE} = \gamma_{RF} = 0°$).

(a) $\gamma_{Aft} = -45°$, $\alpha = 4°$

(b) $\gamma_{Aft} = -45°$, $\alpha = 8°$

(c) $\gamma_{Aft} = -0°$, $\alpha = 4$

(d) $\gamma_{Aft} = -0°$, $\alpha = 8°$

(e) $\gamma_{Aft} = -45°$, $\alpha = 4°$

(f) $\gamma_{Aft} = -45°$, $\alpha = 8°$

Figure 9. Attainable pitching moments from experimental and numerical data (VLM, RANS and wind-tunnel tests at Re = 3·18 x 10^5) at 4° and 8° angle-of-attack for $\gamma_{LF} = 0°$, $\gamma_{Aft} = \{-45°, 0°, +45°\}$, and [−90°, 90°] (the angle-of-attack value effectively used during the VLM and RANS computations was adjusted so that the observed and predicted lift coefficients match when $\gamma_{LE} = \gamma_{RF} = 0°$).

(a) Lift
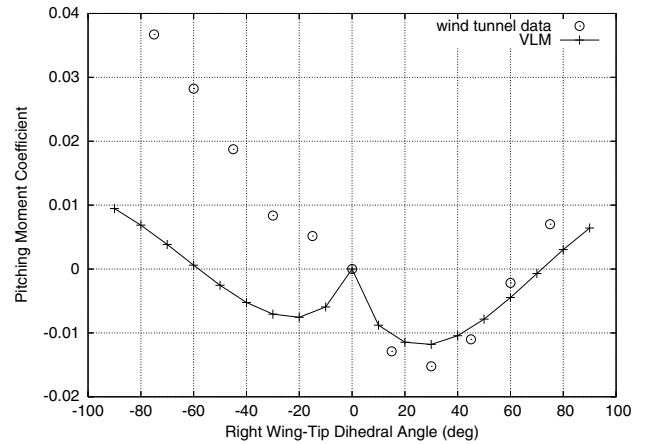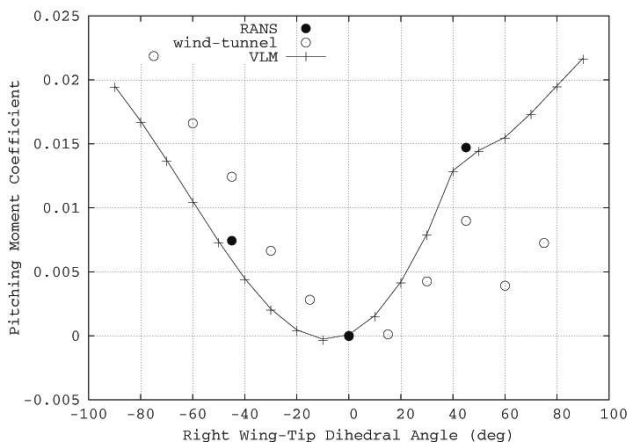

(b) Drag Variation

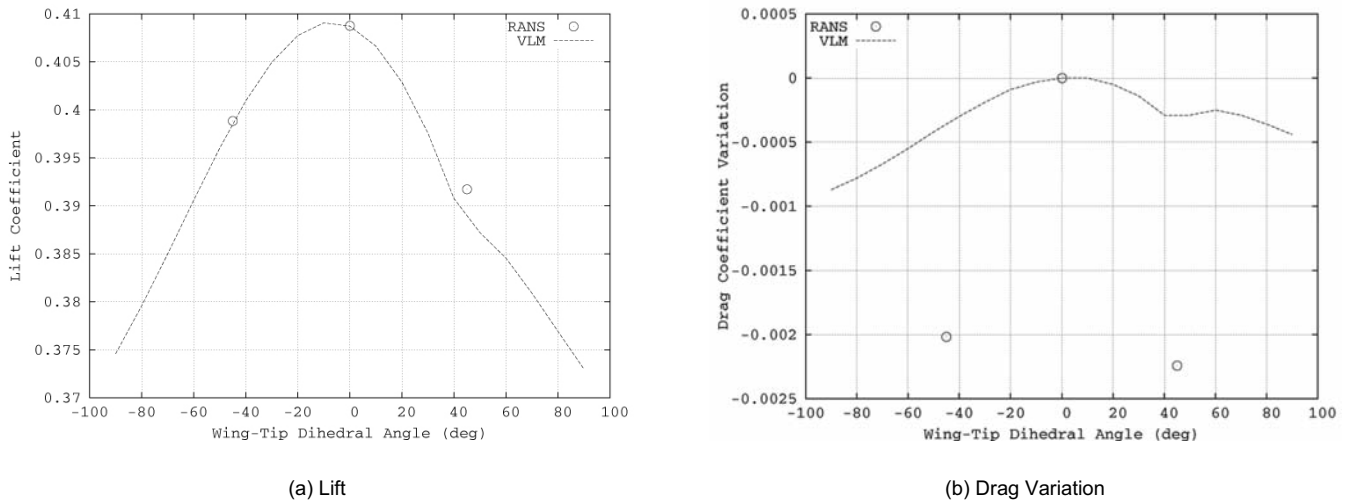Figure 10. Lift and drag variations with respect to γ_{RF}, when $\gamma_{RF} = 0°$ and $\gamma_{Aft} = 45°$. Predicted VLM drag is lift-induced drag, whereas predicted RANS drag is viscous drag plus lift-induced drag. Drag is given in terms of increment with respect to the case where $\gamma_{RF} = \gamma_{RF} = 0°$, $\gamma_{Aft} = 45°$.

camber of the main wing so that the whole configuration is naturally trimmed at that intermediate dihedral angle), one can nose up (respectively, down) the flying wing by increasing (respectively, decreasing) at a fixed angle-of-attack the magnitude of the dihedral angle about this intermediate position. Similarly, if the angle of attack is allowed to change to accommodate to a new flight condition, decreasing (respectively, increasing) the absolute amount of aft wing-tip dihedral will trim the aircraft at a greater (respectively, smaller) flight speed.

4.1.2 Lateral/directional control

With the aft winglets deflected in tandem at a given dihedral angle so as to trim the flying wing longitudinally, roll and yaw can be created by deflecting one of the fore winglets off the wing plane. Predicted and observed moments are shown in Figs 7 to 9 for configurations with aft winglets set symmetrically at either –45°, 0° or +45°, left fore winglet fixed in the wing plane and right fore winglet deflected off the wing plane. Whereas VLM computations were performed for all the configurations, RANS computations were only performed for $\gamma_{Aft} = -45°$, $\gamma_{LE} = 0°$ and $\gamma_{RF} = \{+45°; +0°. +30°\}$. All the moments are relative to the configuration with both front winglets in the wing plane.

As far as rolling moments are concerned (Fig. (7)), the agreement between experimental and numerical data is fairly good, except for the configuration with aft winglets fixed in the wing plane, where the VLM predicts negative roll for negative dihedral angles in [0°, –50°] whereas the experiment does not. As expected, a positive rolling control moment is produced, that is the wing will roll to the right (i.e. to the side where the front winglet is off the wing plane), whether the winglet is deflected up or down (however in the particular case with aft winglets in the wing plane, positive dihedral angles need to be greater than 40° ~ 60° for positive roll to be produced – negative roll is produced otherwise!). As far as yawing moments are concerned (Fig. 8), the agreement between experimental and numerical data is also fair. Upward deflection of the right front winglet creates positive yaw (i.e. proverse yaw with respect to the generated roll moment) and vice versa. This effect

was expected since the side-force produced on the deflected fore winglet is acting inward, behind the centre of gravity. Therefore deflecting the front winglet upward from the wing plane is desired if one wants to achieve a co-ordinated turn with the 4-winglet control system. In terms of pitching moments (Fig. 9), the agreement between simulation and experiment is not as good as it was for roll and yaw, nevertheless numerical predictions reproduce the trend of the experimental data: a positive pitch is created (i.e. the flying wing will nose up) when the front winglet is deflected (enough) off the wing plane, which is a positive side-effect since it will help co-ordinate a turn when the wing is banked.

In terms of mathematical modelling, it appears from Figs 7–10 (a) that the reduced-order model (VLM) is accurate enough for predicting the quantities of interest (lift, roll, pitch and yaw) for the investigated concept: RANS numerical flow solutions do not indeed give much improved predictions with respect to the VLM (which are already in good agreement with the wind-tunnel data, except perhaps when the fore and aft wing-tips are in close alignment and the angle of attack is small)[†]. Therefore, the viscous drag, which is accounted for in the RANS approach but not in the VLM, does not contribute significantly to the control moments, despite being the major source of drag variation when the wing-tip dihedral angle is changed (see Fig. 10). On this subject, it is interesting to note that the RANS analysis of the configuration with the leading winglet in plane with the trailing winglet (case $\gamma_{RF} = \gamma_{Aft} = -45°$, $\gamma_{LF} = 0°$) gives roughly as much total drag (within two counts) as the configuration with the leading winglet deflected opposite the trailing winglet (case $\gamma_{RF} = -45°$, $\gamma_{Aft} = 45°$, $\gamma_{LF} = 0°$). This is quite unexpected, due to the significantly different wing-tip arrangements and an expected strong interaction when the fore and aft winglets are in the same plane. Visualisation of the transverse kinetic energy field (an indicator of lift-induced drag – not shown) at a downstream plane perpendicular to the freestream reveal that the configuration with fore and aft winglets in the same plane produce more lift-induced drag (more transverse kinetic energy is released into the wake) than the configuration with fore and aft winglets deflected apart. However, visualisation of the field of total-pressure variation (an indicator of viscous drag, here form drag and skin-friction drag) at

---

[†] The observed kink in the moment coefficient curves, when the fore wing-tip passes in the rear wing-tip plane, is predicted by the VLM as well but not to the same extent, especially when the wing angle of attack is small, see Figs (a) *vs* (b). This might suggest that modelling the wake interference from the leading wing-tip on the trailing wing-tip would be particularly important when both of them are in close alignment. This modelling could be enhanced by replacing the rigid wake model by a force-free wake model within the VLM. However, the RANS method, which intrinsically accounts for the wake roll-up (force-free wake), does not enable improved predictions in the kink region of the moment curves (Figs 8(e) and 9(e)), except maybe in terms of rolling moment – Fig. 7(e).[†]

(a) $\gamma_{LF} = 0°$ $\gamma_{RF} = \gamma_{Aft} = 45°$

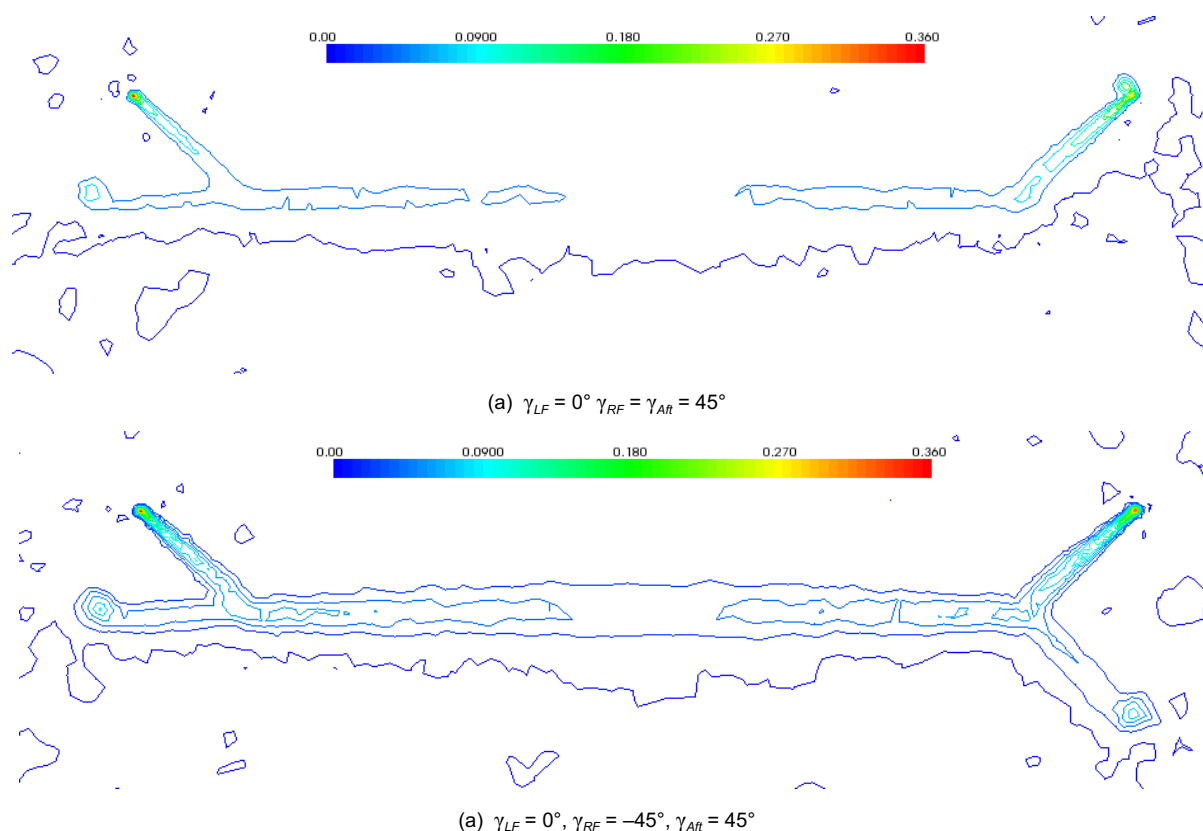(a) $\gamma_{LF} = 0°$, $\gamma_{RF} = -45°$, $\gamma_{Aft} = 45°$

Figure 11. Contours of total-pressure variation (freestream value – local value) normalised by the freestream dynamic pressure, in a plane normal to the freestream velocity, located one winglet-tip chord aft of the rear-winglet tip trailing edge.

the same downstream location indicates that the configuration with fore and aft winglets in the same plane generates less viscous drag: one can indeed see from Fig. 11 that not only the variation of total pressure is weaker for this configuration but also that the zone where this variation occurs, the wake, is smaller (relative to the case with winglets deflected apart) due partly to the wake of the fore winglet impinging on the aft winglet. Since both configurations produce more or less the same amount of drag, we can conclude that the increase in lift-induced drag is approximately balanced by the decrease in viscous drag for the configuration with fore and aft winglets in the same plane, relative to the configuration with winglets deflected apart.

Since the RANS analysis does not provide significant improvements in terms of lift and control moment predictions, further numerical results in the paper will be only based on the VLM.

4.1.3 Improvement of the design

So far the wing-tip aerofoils of the analysed configurations had zero incidence with respect to the main-wing chord line (see Fig. 3). Control authority in pitch can be improved by tilting the aft wing-tips forward (i.e. decreasing their incidence), so that they have a nose-down attitude with respect to the main wing. Similarly, the wing-tip effectiveness in producing roll and/or yaw can be improved by tilting the fore wing-tips backward so that they have a nose-up attitude with respect to the main wing. To check this, configurations with a 5° positive incidence on the fore wing-tips and/or a 5° negative incidence on the aft wing-tips have been analysed numerically and compared to their counterparts with zero incidence. Results in terms

of reduced roll rates[†] are shown in Fig. 12 for the configurations with aft winglets at +45°. It can be seen from this figure that the positive incidence of the fore winglets increases the roll rate by about 20% at dihedral angles greater than 40°. With regard to the negative incidence of the aft winglets, one can also see that it has no significant influence on the roll rate.

The computed aft wing-tip dihedral angles to trim the flying wing in straight flight at various lift coefficients (while both fore wing-tips are planar) are shown in Fig. 13. Again the configuration with aft and fore winglets tilted apart is the most effective, allowing a wider range of lift coefficients in trimmed flight to be attained.

4.1.4 Comparison to wing-tip tilting

The effectiveness of the folding fore winglets with regard to rolling is assessed by comparing them to fixed-dihedral-angle, tiltable fore winglets (i.e. their incidence can be changed w.r.t the main wing). The predicted reduced roll rates for both roll control systems are shown in Fig. 14. One can immediately notice that the roll effectiveness of the folding winglet depends on the operating lift coefficient (the greater, the better) whereas for the tilting winglets, it does not. The range of incidence for the tilting wing-tips has been limited to ±10 relative to the wing chord line because it can be safely assumed that outside this interval the tilted wing-tips would be stalled and the roll effectiveness would decay. Besides, inside this interval, the VLM can be used to give a fair estimate of the maximum roll rate because attached flow prevails on the tilted lifting surfaces. The folding winglet does not suffer from this stall limitation, since deflecting the winglet off the wing plane will decrease its effective

[†]The reduced roll rate was computed using the following formula: $\hat{p} = -C_{l\omega}/C_{lp}$, which is obtained from the equations governing the rotary motion of the wing by assuming one rotational degree of freedom and solving for the steady state. $\hat{p} = pb/2V_{cg}$ is the dimensionless roll rate, $C_{l\omega}$ is the rolling moment that initiated the roll (rolling moment due to the rotation of the right fore winglet), and C_{lp} is the damp-in-roll derivative about the state that initiated the roll. $C_{l\omega}$ and C_{lp} were obtained on the basis of steady-state aerodynamics by using the VLM.
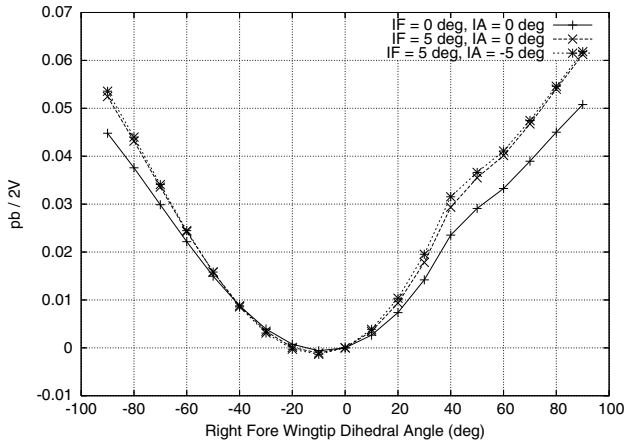
Figure 12. Effect of the winglet incidence on the steady-state roll rate (VLM predictions; C_{L_0} = 0·6; IF and IA refer respectively to the incidence of the fore and aft winglets).
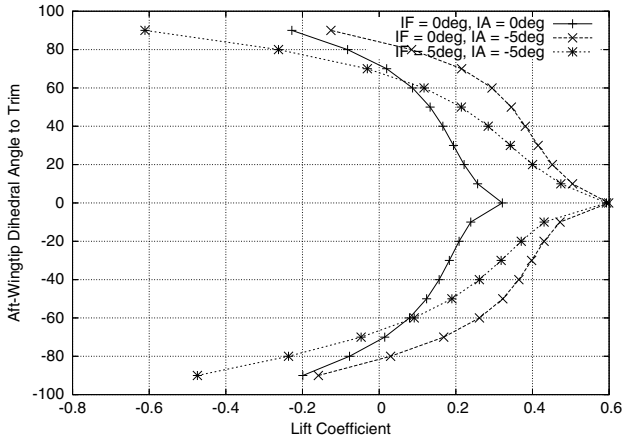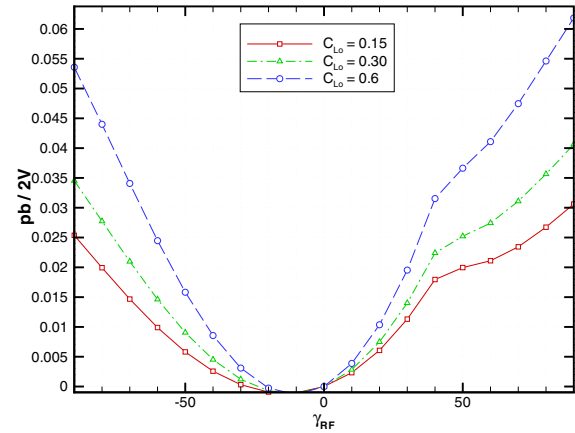

(a) Folding

Figure 13. Aft-winglet dihedral angles to trim the flying wing longitudinally (VLM predictions; $\gamma_{LF} = \gamma_{RF}$ = 0°; aft winglets symmetrically deflected; IF and IA refer respectively to the incidence of the fore and aft winglets). For each γ_{Aft}, the angle-of-attack was adjusted during the computation so as to zero out the pitching moment.

(b) Tilting

Figure 14. Steady-state, dimensionless roll rates attainable by: (a) varying γ_{RF} while γ_{LF} = 0° (incidence of both fore winglets is fixed at +5° with respect to wing chord); (b) varying the fore winglet incidence with respect to the wing chord (left and right winglets are tilted apart, with left one nosing up and right one nosing down). VLM predictions; in all cases γ_{Aft} = 45° and aft winglet incidence is of −5°; CL0 refers to the lift coefficient of the configuration when both fore winglets are at zero dihedral angle (folding winglet case) or at zero incidence with respect to the wing chord (tilting winglet case).
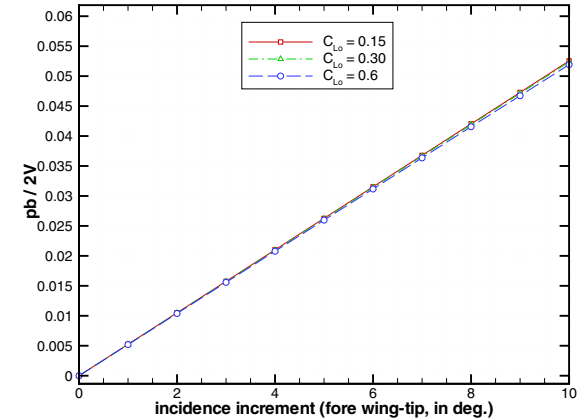
angle of attack, diminishing therefore the risk of stall (that is why VLM predictions match experimental data quite well even for large deflections). Bearing all of this in mind, it appears that tilting wing-tips are only superior to folding wing-tips at low lift coefficients (for instance, at C_L = 0·15, maximum dimensionless roll rate is 0·05 for the titling wing-tips and 0·03 for the folding wing-tips). Hence folding wing-tips are more suitable at low speed for roll control.

4.1.5 Compressibility effects

To extend the VLM to compressible flows (purely subsonic), the Prandtl-Glauert similarity rule is applied. The predicted trend of the maximum roll rate at fixed lift coefficient is plotted versus the Mach number in Fig. 15 (given the LE sweep angle of 30° and the moderate aerofoil thickness, it is reasonable to assume the Prandtl-Glauert correction valid up to Ma = 0·7). It can be seen that the

maximum roll rate decreases slightly with the Mach number (10% drop between Ma = 0 and Ma = 0·7 at C_L at 0·6), this effect is less pronounced for smaller lift coefficients though.

4.2 Simulation of a level turn

The split-tip flying wing configuration was numerically analysed with the VLM in a turning, incompressible airflow simulating a steady level turn governed by the following algebraic equations:

$$
\begin{aligned}
V_{cg} &= \sqrt{2W/(\rho C_{L_0} S)} \\
C_L &= C_{L_0}/\text{Cos}\phi \\
R &= V_{cg}^2/g\text{Tan}\phi \\
\Omega &= V_{cg}/R
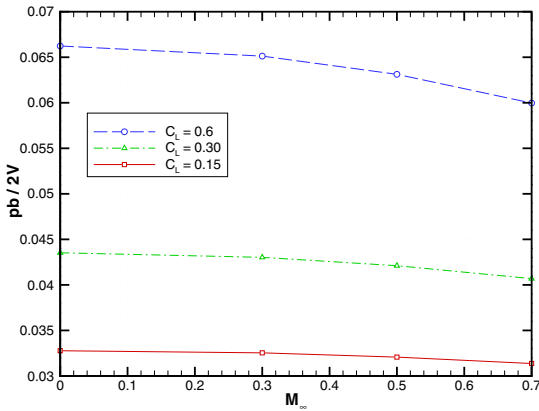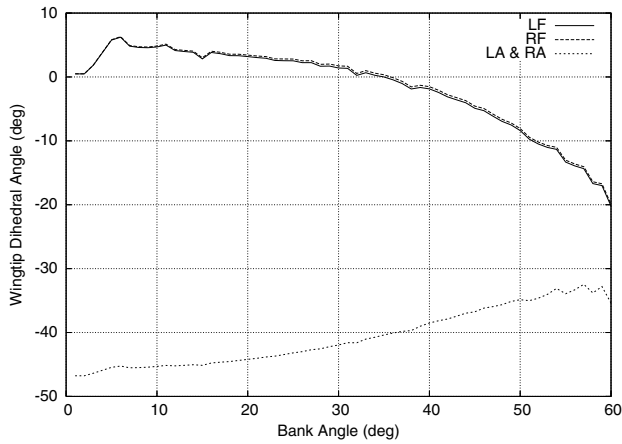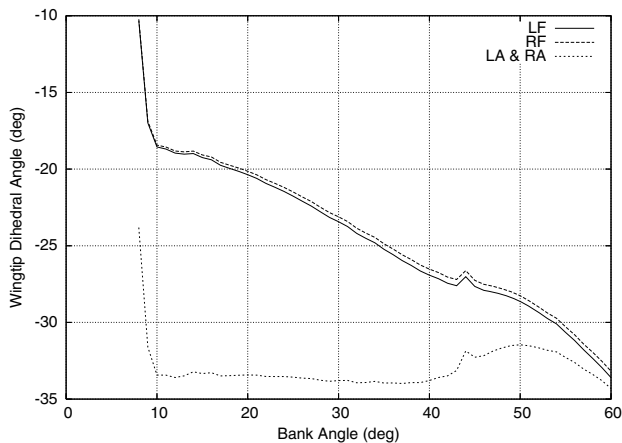\end{aligned}
\qquad \ldots (1)
$$

Figure 15. Predicted trend of the steady-state, dimensionless roll rate when the Mach number increases for the configuration featuring $\gamma_{Aft} = 45°$, $\gamma_{LF} = 0°$, and $\gamma_{RF} = 90°$.

(a) $C_{L0} = 0.2$

(b) $C_{L0} = 0.4$

Figure 16. Control angles for the morphing flying wing to sustain a level turn at a given bank angle (VLM simulations; C_{L0} is the lift coefficient upon initiation of the level turn from a straight, level flight). LF, RF, LA and RA refer respectively to the Left Fore, Right Fore, Left Aft and Right Aft winglet dihedral angles.

R turn radius S reference wing area V_{cg} velocity of the wing centre of gravity W aircraft weight g gravitational acceleration turn rate air density;

$$\begin{aligned} p &= 0 \\ q &= \Omega \sin\phi \\ r &= \Omega \cos\phi \end{aligned} \qquad \dots (2)$$

where C_{L0} is the lift coefficient at zero bank angle, that is in straight level flight, upon initiation of the turn. Rotation rates were directly constrained through the prescribed bank angle and turn rate. The sideslip angle was fixed to zero. The control angles, γ_{LF}, γ_{RF}, γ_{Aft}, required to zero out the aerodynamic moments during the turn[†] and the angle of attack, α, required to maintain the lift coefficient prescribed from Equation (1) are obtained by solving the corresponding moment and lift equality constraint equations with Newton's method. The Newton step is obtained by solving the following linear system:
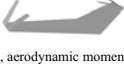
$$\begin{pmatrix} C_{L_\alpha} & C_{L_{\gamma_{LF}}} & C_{L_{\gamma_{RF}}} & C_{L_{\gamma_{Aft}}} \\ C_{l_\alpha} & C_{l_{\gamma_{LF}}} & C_{l_{\gamma_{RF}}} & C_{l_{\gamma_{Aft}}} \\ C_{m_\alpha} & C_{m_{\gamma_{LF}}} & C_{m_{\gamma_{RF}}} & C_{m_{\gamma_{Aft}}} \\ C_{n_\alpha} & C_{n_{\gamma_{LF}}} & C_{n_{\gamma_{RF}}} & C_{n_{\gamma_{Aft}}} \end{pmatrix} \begin{pmatrix} \Delta\alpha \\ \Delta\gamma_{LF} \\ \Delta\gamma_{RF} \\ \Delta\gamma_{Aft} \end{pmatrix} = \begin{pmatrix} C_L - C_L^* \\ -C_l^* \\ -C_m^* \\ -C_n^* \end{pmatrix} \qquad \dots (3)$$

The Δ's symbolise the corrections to be added to the current estimates of angle-of-attack and control angles. The starred aerodynamic coefficients and the stability derivatives are evaluated at the current operating point (i.e. for the current estimates of control angles and angle-of-attack). The system is updated until the Newton step becomes smaller than a prescribed tolerance. Converged results for C_{L0} values of 0.2 and 0.4 are plotted in Fig. 16 against the bank angle. Note that the fore winglets are always almost symmetrically deflected to trim the flying wing during the turn. Because the system of constraint equations is non-linear, there are multiple solutions[‡] satisfying the constraints, as shown in Table 1; this allows for the optimisation of a secondary objective function, such as minimum induced drag or minimum deflection, for instance. Results plotted in Fig. 16 have in fact been obtained by retaining among the multiple solutions only the combinations of dihedral angles leading to maximum span; such combinations should tend to minimise the induced drag during the turn.

5.0 CONCLUSION

A novel control method based on independently-actuated, articulated, split wing-tips was investigated. Observed and predicted control moments about the three axes were in good agreement and demonstrated that the proposed control effectors could generate proverse, multi-axis moments. In fact, multiple solutions exist to generate one set of control moments at a given flight point, which allows for the optimisation of a second objective function, such as minimum drag for instance. It was also shown that the control

Table 1
Different combinations of wing-tip dihedral angles trimming the flying wing at 30° bank angle for a flight speed of $V_{cg} = \sqrt{10W/(\rho S)}$

Geometry	α (deg)	γ_{LF} (deg)	γ_{RF} (deg)	γ_{Aft} (deg)	C_{D_i}
	2·66	2·34	2·69	−41·60	0·0057
	2·77	−54·10	−53·81	68·41	0·0062
	3·62	169·80	169·66	142·99	0·0089

[†] Limiting consideration to the case of small turn rates (i.e. $b \ll 2R$), and assuming the thrust line passes through the aircraft CG, aerodynamic moments about the aircraft CG are zero to the first order in rotation rates.

[‡] Those multiple solutions were obtained by changing the initial estimate of the control angles in Newton's method.

system was more effective than a more conventional one at moderate and high lift coefficients, so it could be applied effectively to low-speed or high-altitude morphing aircraft.

ACKNOWLEDGMENTS

REFERENCES

1. CULICK, F.E.C. The Wright Brothers: First Aeronautical Engineers and Test Pilots, *AIAA J*, **41**, No 6, June 2003, pp 985-1006.

2. JHA, A.K. and KUDVA, J.N. Morphing aircraft concepts, classifications and challenges, *Structures and Materials* 2004: Industrial and Commercial Applications of Smart Structures Technologies, Proceedings of SPIE, **5388**, pp 213-224.

3. Sanders, B., Eastep, F.E. and Forster, E. Aerodynamic and aeroelastic characteristics of wings with conformal control surfaces for morphing aircraft, *J Aircr*, January–February 2003, **40**, (1), pp 94–99.

4. HALL, J.M., Executive Summary AFTI/F-111 Mission Adaptive Wing, WRDC-TR-89-2083, September 1989.

5. KHOT, N.S., ZWEBER, J.V., VELEY, D.E., OZ, H. and EASTEP, F. E., Flexible composite wing with internal actuation for roll manoeuvre, *J Aircr*, July–August 2002, **39**, (4), pp 521-527.

6. NATARAJAN, A., KAPANIA, R.K. and INMAN, D.J. Aeroelastic optimization of adaptive bumps for yaw control, *J Aircr*, January-February 2004, **41**, (1), pp 175-185.

7. NEAL, D.A., GOOD, M.G., JOHNSTON, C.O., ROBERTSHAW, H.H., MASON, W.H. and INMAN, D.J. Design and wind-tunnel analysis of a fully adaptive aircraft configuration, AIAA Paper 2004-1727, April 2004.

8. BAE, J.S., SEIGLER, T.M. and INMAN, D.J. Aerodynamic and static aeroelastic characteristics of a variable-span morphing wing, *J Aircr*, 2005, **42**, (2), pp 528-534.

9. HENRY, J.J., BLONDEAU J.E. and PINES, D.J. Stability analysis for UAVs with a variable aspect ratio wing, AIAA Paper 2005-2044, April 2005.

10. SEIGLER, T.M., NEAL, D.A., BAE, J.S. and INMAN, D.J., Modelling and flight control of large-scale morphing aircraft, *J Aircr*, 2007, **44**, (4), pp 1077-1087.

11. CAMPANILE, L.F. Lightweight Shape-Adaptable Aerofoils: A New Challenge for an Old Dream, Adaptive Structures: Engineering Applications, Ed by WAGG, D., BOND, I., WEAVER, P. and FRISWELL, M., John Wiley & Sons, Chicester, UK, 2007, pp 89-135.

12. LU, K. J. and KOTA, S. Design of Compliant Mechanisms for Morphing Structural Shapes, *J Intelligent Material Systems and Structures*, 2003, **14**, (6), pp 379-391.

13. BOURDIN, P., GATTO, A. and FRISWELL, M. I. Aircraft control via variable cant-angle winglets, *J Aircr*, March-April 2008, **45**, (2), pp 414-423.

14. SAFFMAN, P.G. *Vortex Dynamics*, Cambridge University Press, 1992, pp 46–48.

15. WELLER, H.G., TABOR G., JASAK H. and FUREBY C. A tensorial approach to computational continuum mechanics using object-oriented techniques, *Comput Phys*, 1998, **12**, (6), pp 620–631.

16. PATANKAR, S.V. *Numerical Heat Transfer and Fluid Flow*, McGraw-Hill, 1980.

17. SPALART, P.R. and ALLMARAS, S.R. A one-equation turbulence model for aerodynamic flows, *La Recherche Aerospatiale*, 1994, **1**, pp 5–21.

18. VASSBERG, J.C., DEHAAN M.A. and SCLAFANI, T.J., Grid generation requirements for accurate drag predictions based on OVERFLOW Calculations, AIAA paper 2003-4124, 2003.

19. MUELLER, T.J. Aerodynamic measurements at low Reynolds numbers for fixed wing micro-air vehicles, RTO AVT/VKI special course on development and operation of UAVs for military and civil applications, 1999.